Strain-induced accelerated asymmetric spatial degradation of polymeric vascular scaffolds

Pei-Jiang Wang[a,b,1], Nicola Ferralis[c], Claire Conway[a], Jeffrey C. Grossman[c], and Elazer R. Edelman[a,d]

[a]Institute for Medical Engineering & Science, Massachusetts Institute of Technology, Cambridge, MA 02139; [b]Department of Biomedical Engineering, Boston University, Boston, MA 02215; [c]Department of Materials Science and Engineering, Massachusetts Institute of Technology, Cambridge, MA 02139; and [d]Cardiovascular Division, Department of Medicine, Brigham and Women's Hospital, Harvard Medical School, Boston, MA 02115

Polymer-based bioresorbable scaffolds (BRS) seek to eliminate long-term complications of metal stents. However, current BRS designs bear substantially higher incidence of clinical failures, especially thrombosis, compared with metal stents. Research strategies inherited from metal stents fail to consider polymer microstructures and dynamics—issues critical to BRS. Using Raman spectroscopy, we demonstrate microstructural heterogeneities within polymeric scaffolds arising from integrated strain during fabrication and implantation. Stress generated from crimping and inflation causes loss of structural integrity even before chemical degradation, and the induced differences in crystallinity and polymer alignment across scaffolds lead to faster degradation in scaffold cores than on the surface, which further enlarge localized deformation. We postulate that these structural irregularities and asymmetric material degradation present a response to strain and thereby clinical performance different from metal stents. Unlike metal stents which stay patent and intact until catastrophic fracture, BRS exhibit loss of structural integrity almost immediately upon crimping and expansion. Irregularities in microstructure amplify these effects and can have profound clinical implications. Therefore, polymer microstructure should be considered in earliest design stages of resorbable devices, and fabrication processes must be well-designed with microscopic perspective.

bioresorbable scaffolds | Raman spectroscopy | microstructure heterogeneities | polymer degradation | structural deformation

Cardiovascular diseases remain the primary cause of morbidity and mortality globally (1) although at declining rates due to the refinement in vascular interventions. Bare metal stents open narrowed vessels by providing permanent radial support to the arterial wall. However, they are overcome by tissue hyperplasia that reobstructs the lumen creating clinical restenosis (2, 3). Drug-eluting stents (DES) release antiproliferative drugs from polymer coatings on stent struts suppressing this overgrowth (4, 5), and they have been extremely successful in restoring vascular flow. But, metal endovascular stents are still permanent foreign objects residing inside arteries, raising concern that they will forever impede full vascular repair, leaving the artery exposed to chronic reactivity, vessel caging, limited reintervention, alteration of vasomotor tone, and vessel rupture from strut fracture (6–8). Metal stents thus relegate patients to lifelong need for vigilant adherence to complex drug regimens and concern for thrombosis (4, 5, 9). These fundamental limitations associated with metal stents are why the community looked to bioresorbable scaffolds (BRS) for relief. BRS are designed to provide temporary vascular radial support, slowly disappearing, theoretically reducing long-term complications with permanent implants. However, mounting clinical evidence shows increased thrombosis, especially during acute time settings (10–12). BRS implanted arteries clot at a two- to threefold higher rate than with DES, inducing more myocardial infarctions (13, 14). Despite corrective strategies focusing on optimizing implantation with pre- and postimplantation dilation, negative results abound. Early loss of scaffold integrity including circumferential and longitudinal compression as well as

malapposition (15), and nonsuperior vasomotion recovery with respect to metal stents at 3 y, when scaffolds should be completely degraded and absorbed, point to microscopic material and issues related to scaffold design and features rather than technique limitations (14, 16). However, until now, the materials mechanisms responsible for BRS degradation have not been fully presented or understood, limiting not only our understanding of their performance but also predictable quantification of the occurrence of clinical failures. We have relied on a nomenclature and anticipated evidence for failure from the metal stent performance and this is not appropriate. Failure modes for polymer and metal implants are not the same.

Poly-l-lactic acid (pLLA) is most commonly used for BRS by virtue of its mechanical strength, controllable degradation rate, and degradation products (17–19). Fabrication and implantation techniques for BRS are generally similar to those employed for metal stents and include tube extrusion and expansion, laser cutting, drug/polymer coating, crimping, sterilization, and deployment (20, 21). However, unlike metals, semicrystalline polymers like pLLA possess entirely different microstructures such as crystal domains where molecules are differentially aligned, and packed and amorphous regions where molecules are randomly oriented. These microstructures can profoundly affect macroscopic properties, such as mechanical strength and degradation (22–24). Each step in scaffold fabrication and implantation

Significance

Bioresorbable scaffolds (BRS) were thought to represent the next cardiovascular interventional revolution yet they failed compared with metal stents. When BRS were tested using methods for MS, no signal of concern emerged—perhaps because BRS are not metal stents. BRS not only degrade, they also possess significant localized structural irregularities that cause asymmetric degradation. We posit these microstructural irregularities are responsible for variability in device performance in first-generation BRS. We correlated nonuniform degradation with variation in polymer microstructure and tolerance to integrated strain generated during fabrication and implantation. Differentiating failure modes in metallic and polymeric devices explains clinical results and suggests optimization strategies for the design and fabrication of next-generation BRS, indeed all devices using degradable materials.
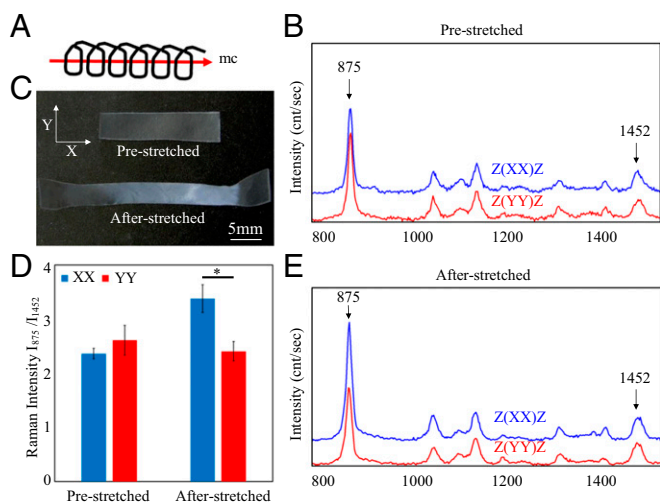
Fig. 1. Changes in molecular orientation identified with polarized Raman spectroscopy on stretched pLLA sheets. (*A*) mc axis. (*B* and *E*) Polarized Raman spectra of pre- and after-stretched pLLA sheets from 800 to 1,500 cm-1. (*C*) Pre- and after-stretched pLLA sheet. (*D*) Changes in intensity ratio with different polarization geometry: $I_{875}/I_{1,452}$ was not statistically different before being stretched (*XX* vs. *YY*, mean ± SD, 2.4 ± 0.10 vs. 2.6 ± 0.28, P = 0.172), and becomes much higher (*XX* vs. *YY*, mean ± SD, 3.4 ± 0.26 vs. 2.4 ± 0.18, P = 0.0075) with $Z(XX)Z$ compared with $Z(YY)Z$ after being stretched in the *X* direction. This implies the molecules are aligned more toward the drawing direction. Based on Porto's notation (28), *XX* and *YY* indicate that the polarization of the incident beam was parallel to that of the analyzed beam. n = 6 for each scenario.

produces unique strain fields which induce localized microstructural anisotropy and changes in macroscopic performance (25). It is critical to characterize microstructures within devices to predict overall performance. However, such characterizations are often ignored during device design and fabrication from limitations on the scale resolution of standard methods, such as gel permeation chromatography and differential scanning calorimetry (DSC). Lack of such information produces unpredictable results in vivo.

With Raman spectroscopy as a quantitative tool with microscale resolution, we analyzed microstructures including distribution of polymer molecular orientations and crystallinity within scaffolds. We identified spatial heterogeneities in microstructures within these devices. We directly connected microscopic scaffold properties with macroscopic properties, and revealed that strain-induced heterogeneity in alignment and crystallinity leads to increased localized degradation and loss of structural integrity well before chemical processes can emerge and along a timeline that follows that of premature clinical failure.

Results

Quantification of pLLA Sheets Orientation Using Polarized Raman Spectroscopy.
We examined clinical-grade BRS scaffolds and sheets of the same pLLA to define material orientation. The pLLA polymer helical structure (26) can be represented with mc axis, defined as the molecular chain axis (Fig. 1*A*). The integrated intensity of the Raman band at 875 cm^{-1} (I_{875}, Fig. 1*B*) represents the stretch mode of C-COO, the polymer backbone (27). As the polymer chain increases and becomes preferably aligned in one direction, the stretch of an extended backbone will result in an amplified signal in response to the incident polarized light, and thus I_{875} will also be stronger (28). During degradation, the cleavage of C-COO destroys the alignment of the polymer chain and reduces the synchronization of the stretch mode—accordingly, the corresponding Raman band intensity also falls. The integrated

intensity of the Raman band at 1,452 cm^{-1} ($I_{1,452}$, Fig. 1*B*) represents the asymmetric bending mode of CH_3 (27) which was considered as an internal standard during degradation (29, 30).

Solvent-casted pLLA sheets were stretched to a strain of 100% (Fig. 1*C*), where the stretch axis was parallel to the polarization axis *X*. In the prestretched sample, the intensity ratio ($I_{875}/I_{1,452}$) with polarization geometry $Z(XX)Z$ [based on Porto's notation (31)] is similar to that with $Z(YY)Z$ [Fig. 1 *B* and *D*, higher with $Z(YY)Z$, but not statistically significant, P = 0.172]. Thus, molecules in the prestretched sample produced through solvent casting at room temperature and pressure were more randomly oriented and isotropic compared with those of the after-stretched sample. After stretch, molecules were aligned in the stretching direction (Fig. 1 *D* and *E*, P = 0.0075), supporting use of $I_{875}/I_{1,452}$ as a marker for molecular orientation.

Quantification of BRS Orientation Using Polarized Raman Spectroscopy.
Scaffolds were positioned with their axial direction (Fig. 2*A*) parallel to the incident light polarization axis *X* (Fig. 2*B*). The scaffold outer surface (OS, surface that contacts vessel walls), the inner surface (IS, surface that contacts luminal flow), and the core (the interior cross-section, Fig. 2*C*) of as-cut scaffolds were examined with polarized Raman spectroscopy (Fig. 2*D*).

For the OS, $I_{XX} > I_{YY}$ (P < 0.001) indicating that polymer strands are substantially more aligned in the axial direction. For the IS, $I_{YY} > I_{XX}$ (P < 0.001), implying that molecules are aligned more toward the circumferential direction. For the core, the differences between the intensities of all three polarization geometries are much less significant compared with the surfaces, with the axial direction being the highest but not statistically significant (P = 0.124 for I_{XX} and I_{RR}). This implies that molecules in the core are more isotropically distributed. The boundary between the core and the surface is at least at about 1 μm below the surface, as that is the penetration depth of the laser. The immediate consequence of the observed heterogeneity in molecular orientation is the
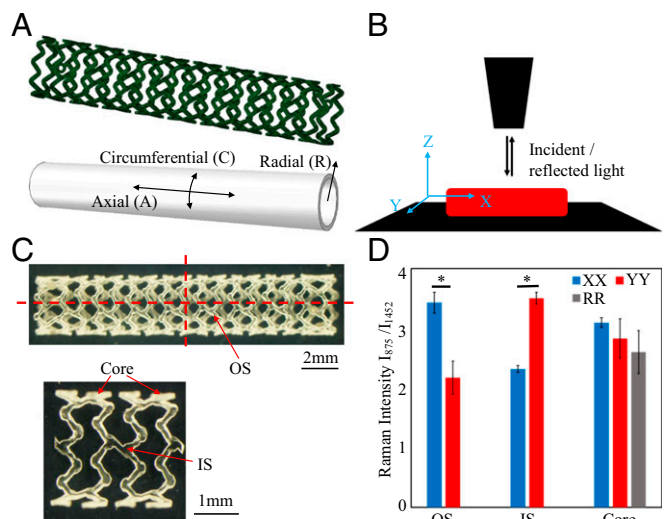

Fig. 2. Quantification of BRS orientation using polarized Raman spectroscopy. (*A*) Scaffolds coordinates: *A*-*C*-*R*. (*B*) Polarized Raman spectroscopy coordinates: *Z* is the direction of the incident light, *X* and *Y* are the polarization axes. (*C*) Scaffolds were cut to expose the core and IS for Raman spectroscopy. (*D*) $I_{XX} > I_{YY}$ (mean ± SD, 3.4 ± 0.17 vs. 2.2 ± 0.28, P < 0.001) on OS indicating molecules are aligned more toward the axial direction. $I_{YY} > I_{XX}$ (mean ± SD, 2.3 ± 0.06 vs. 3.5 ± 0.10, P < 0.001) on IS indicates molecules are aligned more toward the circumferential direction. The core is more isotropic compared with the surfaces (I_{XX} vs. I_{YY} vs. I_{RR}, mean ± SD, 3.1 ± 0.08 vs. 2.8 ± 0.33 vs. 2.6 ± 0.36, P = 0.124 and 0.146 when comparing I_{RR} with I_{XX} and I_{YY}, respectively). n = 6 for each scenario.

APPLIED PHYSICAL SCIENCES

BIOPHYSICS AND COMPUTATIONAL BIOLOGY

spatial heterogeneity in macroscopic properties such as degradation rate and mechanical strength of the scaffold.

In particular, crimping and reinflation were investigated to determine their effects on molecular orientation. All edges were smooth in the as-cut samples (Fig. 3A). Localized deformations were clearly visible at the inner peak edge after crimping (Fig. 3B). After reinflation, localized dimples were found at the outer peak edge and deformations on the inner side were developed into microcracks (Fig. 3C). These locations correspond to regions predicted by finite-element analysis (FEA) on a peak feature after crimping and reinflation where high strain was experienced (Fig. 3E). $I_{875}/I_{1,452}$ with $Z(XX)Z$ polarization geometry decreases ($P = 0.04$), indicating a disruption in the alignment of molecules and the achievement of an orientation-disordered polymer distribution (Fig. 3D). Thus, inhomogeneous, realistic strain fields disrupt the polymer molecular orientation, leading to an increase in the amorphous character of the polymer matrix.

Quantification of BRS Crystallinity Using Raman Spectroscopy. The integrated intensity of the Raman band at 925 cm^{-1} (CH$_3$ rocking mode mixed with the stretch mode of the backbone) was associated with the crystalline phase of pLLA (26). Fig. 4A shows the Raman spectra of two samples with different crystallinity (%CR) verified by DSC (low %CR = 35%, high %CR = 55%) where a stronger peak at 925 cm^{-1} was observed in the high %CR sample. Using the Raman band at 1,452 cm^{-1} (CH$_3$ asymmetric bending mode) taken as an internal normalization standard (29, 30), the $I_{925}/I_{1,452}$ ratio in relation with the nominal values of %CR were used to establish a direct correlation between the Raman spectra for any unknown sample (Fig. 4B). The surfaces (both OS and IS, Fig. 4C) show 61.1 ± 2.8% crystallinity, significantly higher than that of the core (38.3 ± 4.9%, $P < 0.001$). Such distinct difference in the crystal order, along with the molecular orientation, clearly indicates that areas with low %CR and isotropic molecular orientation may have significantly lower molecular density than other regions with high %CR and more
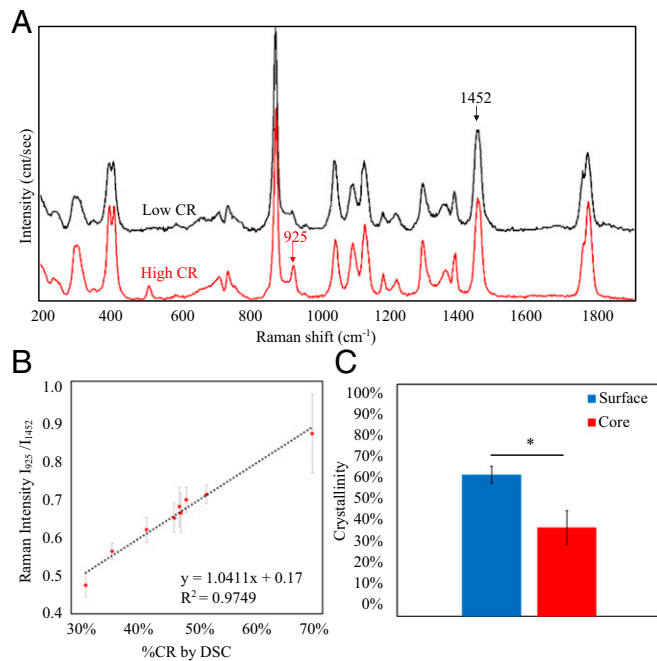

Fig. 4. Quantification of %CR with Raman spectroscopy. (A) Raman spectra of samples with different %CR. (*Top*) Low crystallinity = 35%, weak peak at 925 cm^{-1}. (*Bottom*) High crystallinity = 55%, strong peak at 925 cm^{-1}. (B) Linear relationship between %CR determined by DSC and intensity ratio $I_{925}/I_{1,452}$ determined by Raman spectroscopy. (C) %CR within BRS measured by Raman spectroscopy: significantly higher %CR ($P < 0.001$) on surfaces (mean ± SD, 61.6 ± 2.8%, blue, both OS and IS) compared with that in the core (mean ± SD, 38.3 ± 4.9%, red). $n = 100$ in B. $n = 300$ in C.

anisotropic orientation. Such differentiation is the result of the thermal and mechanical strain history imparted during fabrication and implantation (25, 32), and has significant effects on the macroscopic mechanical properties (22) as well as the degradation rate (33).

Effects of Molecular Structure on Scaffold Degradation and Structural Integrity. Spatial changes in %CR of BRS were examined after static immersion in 37 °C PBS solution (34) for 5, 10, 20, 40, 90, and 110 d using standard curves created above. The %CR on the BRS surface (Fig. 5A) increased from 61.6 ± 2.8% to 71.2 ± 2.6% ($P < 0.001$) in the first 10 d and remained unchanged at ~70.2 ± 3.4% until 90 d. The %CR in the BRS core also increased first, from 38.3 ± 4.9% to 43.7 ± 3.5% in the first 5 d ($P < 0.001$), but then decreased to 29.3 ± 2.8% at 110 d. Localized dimples found at peak features in the scaffold after crimping and reinflation (Fig. 3B) were further enlarged after degradation in 37 °C PBS for 3 mo (Fig. 5B).

The increase in %CR arises from faster degradation in the amorphous regions (a-pLLA) compared with crystalline regions with greater water penetration (35). This change in crystallinity also makes the surface more resilient to hydrolysis than the initial formulation (35) and the core more prone to degradation as it is more amorphous. When degradation byproducts accumulate, local acidity rises accelerating degradation further, which is even heightened in thick first-generation scaffolds (36). In addition to fabrication-induced microstructural differences which led to different degradation rates, structural disruption at peak features in the scaffold that arise from applied strain from crimping and reinflation also promoted the differentiation in microstructure. Furthermore, more significant differences in mechanical strength between the core and the surface result in enhanced formation of geometrical and structural irregularities.
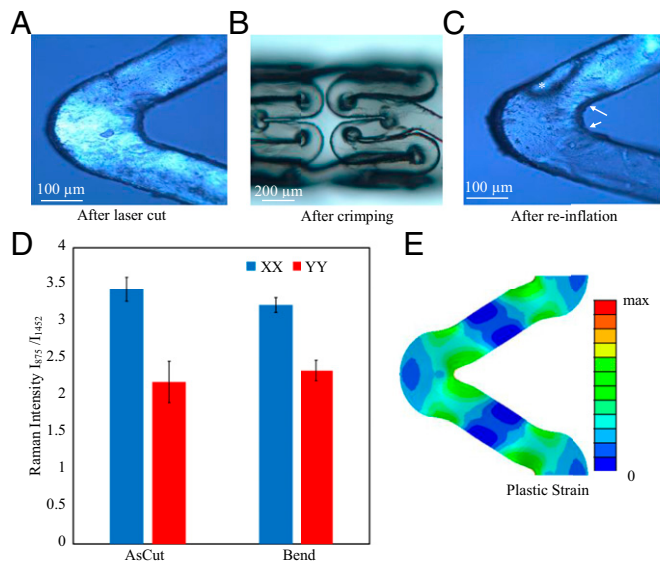

Fig. 3. Crimping and reinflation causing deformations and changes in molecular orientation. (A) Straight edges after laser cut. (B) Localized deformations were seen on the inner peak edges after crimping. (C) Localized deformation (*) and microcrack formation (→) happened at peak features after reinflation. (D) $I_{875}/I_{1,452}$ with $Z(XX)Z$ polarization geometry decreases (mean ± SD, 3.4 ± 0.17 vs. 3.2 ± 0.1, $P = 0.04$) at bend site (*) indicating a disruption in the alignment of molecules. (E) FEA result of plastic strain distribution on a peak feature after crimp and reinflation. $n = 6$ for each scenario.
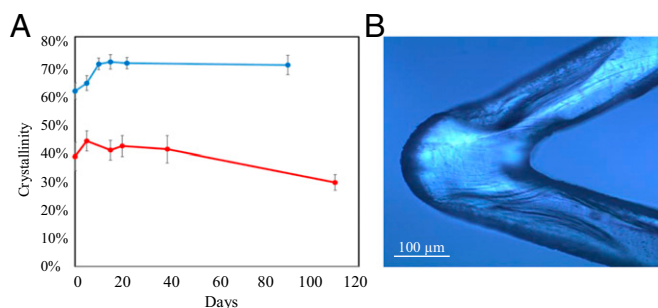
www.manaraa.com

Fig. 5. Heterogeneity in material properties lead to nonuniform degradation and deformation. (*A*) %CR changes slower on surface (blue) compared with those at the core (red). (*B*) Light microscopic view on scaffolds after 3 mo of static immersion in 37 °C PBS indicating severe structural deformation. $n = 300$ in each scenario.

Discussion

Semicrystalline polymer materials like pLLA contain different microstructural environments such as crystal domains and amorphous regions. Macroscopic properties like mechanical strength and material degradation highly depend on their microscopic structures such as molecular orientation and degree of crystallinity (22–24). Typically, increasing crystallinity or molecular orientation will reduce the rate of degradation and increase material stiffness but at the expense of ductility and fragility (23, 24). The introduction of asymmetric spatial degradation calls for refinement of the classic paradigm of resorbable devices (37) (Fig. 6*A*) where scaffold support, material molecular weight, and device mass follow a homogeneous exponential decline. The expectation that material molecular weight changes and overall device mass loss follow a slow continuous course where support is maintained for significant time after implantation well beyond the time of vascular healing is no longer supportable. Asymmetric stresses create discontinuities in resorbable polymeric scaffold integrity far earlier than expected and even before chemical degradation (Fig. 6*B*). When heterogeneous material properties impose asymmetric degradative forces on scaffold struts, mass loss is accelerated and a distribution of degradation emerges which alters the spatial balance of polymer alignment and crystallinity. Loss of support may be subtle at first and does not follow the abrupt discontinuity seen with metal stents, but is during the most vulnerable duration of tissue recovery which might result in acute clinical failures (Fig. 6*C*). Loss of structural integrity is made even more noteworthy once surface crystallinity changes, which might adversely affect endothelial recovery and return of vascular function (14), further increasing clinical complications. Structural failures and resultant clinical implications arise from different mechanical events, on different scales and over different timeframes. One can now well envision how "weak links" in devices can emerge to cause stent failure far earlier than anticipated and why a balanced design must might account for these asymmetries. These issues take on specific urgency for endovascular implants operating in the highly dynamic coronary arterial environment, and in the face of four- to sixfold radial expansion at implantation, added cyclical strain from each heartbeat, and asymmetric recoil and bending forces (32). In BRS, the stakes are even higher for there is as well the dynamic of material degradation linked and matched to the time-evolving aspects of vascular healing. One can no longer expect that the material characteristics guarantee the resorbable scaffolds can maintain mechanical function well beyond vascular repair. There is likely loss of support even during the most critical times of healing and this may then explain in part the unexpected poor results of BVS (Abbott bioresorbable vascular scaffold) in clinical trials.

Wang et al.

Research strategies inherited from metallic stents focus on the evaluation of macrostructural integrity and prevention of abrupt loss due to fracture. Polymeric scaffolds, although rarely fracture, lose their structural integrity early and performance is dominated by microstructural dynamics. Raman spectroscopy defines structural ordering (crystallinity and polymer alignment) with microscale spatial resolution, allowing us to directly identify and correlate the evolution of structural ordering in BRS upon strain application, and the effects on heterogeneous degradation. Significantly higher crystallinity ($61.6 \pm 2.8\%$ vs. $38.3 \pm 4.9\%$, $P < 0.001$) and higher molecular alignment were found on the surface of bioresorbable scaffolds after fabrication than in the core. During crimping and reinflation, the heterogeneous
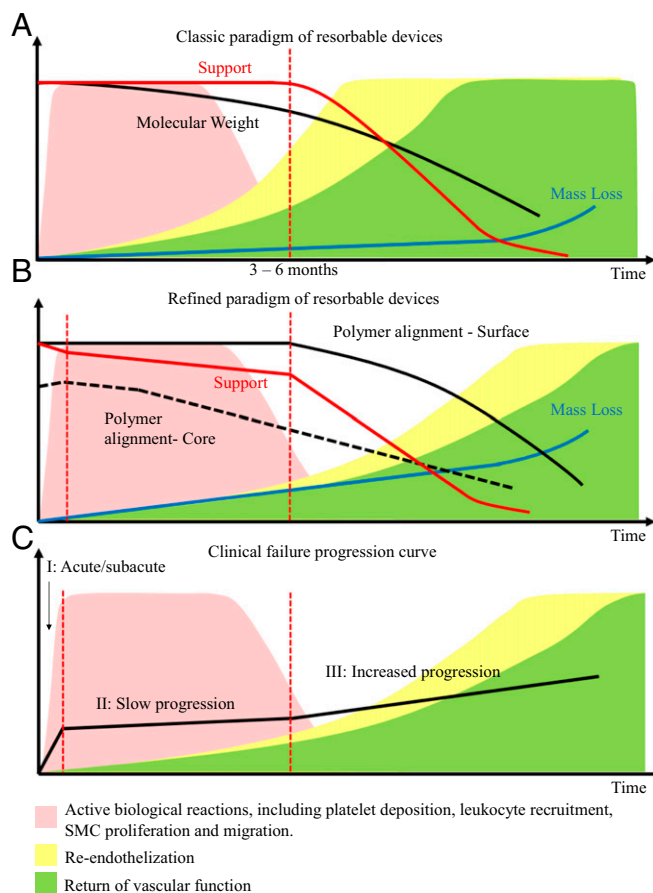

Fig. 6. Theoretical lifespan of bioresorbable devices. (*A*) Classic paradigm of biomaterial resorption. Material molecular weight, support, and mass follow a homogeneous exponential decline. Molecular weight changes smoothly. Mechanical support is maintained for significant time (red dashed line) until active biological reactions (red) have ended and tissues have recovered from intervention due to reendothelization (yellow). Mass loss is delayed until vascular function has returned (green). (*B*) Revised life span of a resorbable scaffold with asymmetric spatial degradation. Low polymer alignment in the scaffold core and asymmetric structural stresses lead to asymmetric degradation which creates early discontinuities in support (red dashed line) and far earlier mass loss—even during periods of tissue vulnerability at heightened inflammation and recovery from implant insult. Reendothelization and the return of vascular function are delayed. Loss of support is even more noteworthy once the surface alignment changes as well. (*C*) Clinical failure progression curve. High rate of clinical failures, especially scaffold thrombosis, occurred during Phase I (acute/subacute, <1 mo) (10) which corresponds to the early loss in scaffold integrity due to asymmetric stresses. Failures slowly progress during Phase II when scaffold core starts to degrade during the most active duration of biological reaction. More failures start to emerge after 3–6 mo (14) which corresponds to the loss in the surface alignment in Phase III.

www.manaraa.com

distribution of strain as dictated by scaffold morphology leads to localized changes in crystallinity and ordering, with an associated reduction in density. Such spatial heterogeneities inevitably produce and localize excess deformations at peak features (Fig. 3 *B* and *C*). Microcracks initiated during crimping indicate potential failure sites which may propagate into macrofractures after implantation under the influence of cyclical strain from the motion of the heart and asymmetric degradation. Dimple deformation initiated during reinflation are therefore indicative of extreme structural irregularities under the influence of degradation. While most of the highly crystalline regions are preserved during strain applications, others undergo structural modifications from high-density crystalline to low-density amorphous, resulting in an enhanced and yet widely heterogeneous degradation. The highly crystalline surfaces of the scaffold could maintain the integrity of their microstructures after being degraded for more than 3 mo. But, the low crystalline core of the scaffold experiences more substantial microstructural disruption with degradation (Fig. 5*A*) accelerated as early as 5 d after fluid contact, unable to maintain a stable mechanical behavior and structural integrity.

The clinical consequences of such a sequence of events are profound. BRS scaffolds are expected to provide stable support for at least 6 mo and longer, and homogeneously across the supported artery and lesion (32). Early loss of stability and uniformity can create the mismatches in alignment of scaffold and artery that we work so hard to avoid. Focal loss of structural integrity can enable greater recoil and malapposition of segments of the scaffold with critical effects on hemodynamics and healing. Protruding struts activate platelets, enable clot formation, delay reendothelization, and could well be responsible for the high risk of thrombosis and myocardial infarction seen with BRS (13, 14, 38, 39).

Thermal and mechanical strain histories imparted during fabrication and implantation (24, 29) have strong and dynamic effects on BRS scaffold microstructure, primarily manifest through the formation of microscale structural heterogeneities. From a materials perspective, we highlight that the strain on the microstructure in pLLA scaffolds directly affects the density of the material at the microscale, with enhanced degradation rates in as-fabricated as well as degraded low-crystalline, low-order regions. The materials-induced structural differentiation in degradation rates is primarily responsible for observed premature degradation potentially leading to unanticipated variability in bioresorbable device performance.

The dynamic and heterogeneous nature of the structural composition not only provides added insight into potential mechanisms of clinical failures in BRS, but points to potential strategies for optimization of design and fabrication of this class of devices and indeed all devices that make use of degradable materials and are subject to continued strain. Fabrication processes, therefore, should be carefully designed to prevent unexpected structural and functional failures. It might well be possible to create microstructure-enhanced polymer scaffolds whose strength matches current metal devices with comparable dimensions, limiting flow recirculation and nonuniform degradation and ultimately associated clinical complications. Controlled degradation through optimized materials and stent design might well result in BRS that are not only competitive with metal stents but overcome their limitations. For example, transitioning from a layered materials design structure (IS, core, OS) to a more homogeneous design would reduce the formation of faster degrading amorphous regions. Alternatively, engineering high-strain regions of the scaffold out of highly crystalline pLLA would mitigate strain-induced changes of the molecular structure toward a-pLLA, and therefore with a homogenization of the degradation rate across the full scaffold. In essence, the design processes should not only consider how the structural profile will affect macroscopic mechanical strength after implantation, but

also should account for how the strain is distributed across the scaffold microstructure. Moreover, scaffolds should not be considered as homogeneous, like metal stents, in computational analyses simulating the mechanical and degradation performance (40–42). Nonuniform properties, such as differential molecular orientation and %CR, should be assigned to OS, IS, and the core of the device to achieve a more valid prediction of performance. With these insights on both micro- and macroscopic perspective, we can now provide a more scientifically driven design and testing paradigm in the development of next-generation BRS specifically and devices of degradable materials in general.

Materials and Methods

pLLA resins, extruded tubes, as-cut scaffold, and fully resorbable pLLA scaffold systems (FRS, Fig. S1) provided by the Boston Scientific Corporation were used in all experimental conditions unless otherwise specified. All units tested were prototypes under development and not commercially available. FRS consists of a catheter, a guide wire, a noncompliant balloon, and a crimped polymeric scaffold. The scaffold is 16 mm in length, 3.0 mm in inner diameter after inflation, and with a wall thickness of 110 μm. Scaffolds were stored at 4 °C until ready for use. Crimping was performed in air at room temperature on as-cut scaffolds. Inflation was performed in a 37 °C water bath within 30 s after immersion. Since the degradation mechanism of PLLA is primarily passive hydrolysis which takes months to years, minimum degradation would have started at this time point. Both as-cut scaffolds and FRS are noncoated.

pLLA Sheets. pLLA resins were dissolved in chloroform and solvent cast into a film with 300-μm thickness at room temperature and pressure. The sheet was cut into 19 × 5-mm rectangles and examined with polarized Raman spectroscopy to determine the molecular orientation before and after 100% strain at 0.1 mm/s over 30 s using a tensile tester (Fig. S2).

Raman Spectroscopy. A Raman spectrometer (Horiba LabRam 800HR) with a 514-nm argon laser was employed. The Raman scatter light was collected through a 100× objective lens, and the intensity was recorded using a CCD camera in the backscattering geometry. Calibration using silicone was done before any measurement. For quantifying %CR on solvent casting films, an area of 20 × 20 μm with 100 data points was measured. Scaffolds were cut to expose the core. Three regions were examined for each scenario (e.g., OS, IS, or the core) and within each region, an area of 20 × 20 μm with 100 data points was measured. For quantifying molecular orientation, polarized Raman spectroscopy was used with three different polarization geometries: Z(XX)Z, Z(XY)Z, and Z(YY)Z [according to Porto's notation (31)] and six replicated measurements were taken on each sample. The spectra were analyzed using Horiba LabSpec (Version 5). Background substation was performed with a degree 3 polynomial function to all spectra before analysis. I_{875} was calculated by integrating from 825 to 900 cm^{-1}. $I_{1,452}$ was calculated by integrating from 1,425 to 1,500 cm^{-1}. I_{925} was calculated by integrating from 910 to 930 cm^{-1}.

FEA. An FEA (Abaqus; Dassault Systemes) was performed to determine high stress–strain locations in the scaffold resulting from the crimp-deploy process. The material model chosen was a Johnson–Cook plasticity model. It was calibrated to uniaxial tension test data obtained from miniature dog bone specimens cut from stent tubing. A single, flat peak of the full scaffold was modeled.

Crystallinity Calibration with DSC. Solvent-cast pLLA film was cut into several 1 cm × 1 cm squares and placed in an 80 °C oven for 0, 5, 10, 30, 60, and 120 min. Percent crystallinity was measured using a TA Instruments Q100 DSC after samples being examined by Raman spectroscopy. Samples were heated at 2 °C/min from 30 to 200 °C. The percent crystallinity was calculated with the equation

$$\%CR = [(H_{melt} - H_{exotherm})/93] * 100\%,$$

where H_{melt} is the area of the melt endotherm, $H_{exotherm}$ is the area under the crystallization exotherm, and 93 J/g is the heat required to melt 100% crystalline pLLA (43). Two DSC measurements were done on each 1 cm × 1 cm square.

Degradation Test on Scaffolds. Scaffolds were inflated and immersed in 37 °C PBS for 5, 10, 20, 40, 90, and 110 d. PBS solution was changed every 2 d to

www.manaraa.com

ensure stable pH at 7.4. At the end of immersion, samples were air dried and mechanically cut for Raman measurement.

Statistical Analyses. Data are presented as mean ± SD unless otherwise specified ($n = 2$ for DSC measurement; $n = 100$ and 300 for %CR measurement on pLLA films and scaffolds using Raman spectroscopy, respectively; $n = 6$ for polarized Raman measurements on molecular orientation). Two-

tailed, unequal variance Student t test were performed and a P value < 0.05 was considered to denote statistical significance.

1. Townsend N, et al. (2016) Cardiovascular disease in Europe: Epidemiological update 2016. *Eur Heart J* 37:3232–3245.
2. Hoffmann R, et al. (1996) Patterns and mechanisms of in-stent restenosis. A serial intravascular ultrasound study. *Circulation* 94:1247–1254.
3. Gordon PC, et al. (1993) Mechanisms of restenosis and redilation within coronary stents–Quantitative angiographic assessment. *J Am Coll Cardiol* 21:1166–1174.
4. Spaulding C, Daemen J, Boersma E, Cutlip DE, Serruys PW (2007) A pooled analysis of data comparing sirolimus-eluting stents with bare-metal stents. *N Engl J Med* 356:989–997.
5. Stettler C, et al. (2007) Outcomes associated with drug-eluting and bare-metal stents: A collaborative network meta-analysis. *Lancet* 370:937–948.
6. Lee MS, et al. (2007) Stent fracture associated with drug-eluting stents: Clinical characteristics and implications. *Catheter Cardiovasc Interv* 69:387–394.
7. Serruys PW, Garcia-Garcia HM, Onuma Y (2012) From metallic cages to transient bioresorbable scaffolds: Change in paradigm of coronary revascularization in the upcoming decade? *Eur Heart J* 33:16–25b.
8. Lee SH, et al. (2007) Frequency of stent fracture as a cause of coronary restenosis after sirolimus-eluting stent implantation. *Am J Cardiol* 100:627–630.
9. Stone GW, et al. (2007) Safety and efficacy of sirolimus- and paclitaxel-eluting coronary stents. *N Engl J Med* 356:998–1008.
10. Capodanno D, et al. (2015) Percutaneous coronary intervention with everolimus-eluting bioresorbable vascular scaffolds in routine clinical practice: Early and mid-term outcomes from the European multicentre GHOST-EU registry. *EuroIntervention* 10:1144–1153.
11. Kraak RP, et al. (2015) Initial experience and clinical evaluation of the Absorb bioresorbable vascular scaffold (BVS) in real-world practice: The AMC Single Centre Real World PCI Registry. *EuroIntervention* 10:1160–1168.
12. Cassese S, et al. (2016) Everolimus-eluting bioresorbable vascular scaffolds versus everolimus-eluting metallic stents: A meta-analysis of randomised controlled trials. *Lancet* 387:537–544.
13. Lipinski MJ, et al. (2016) Scaffold thrombosis after percutaneous coronary intervention with ABSORB bioresorbable vascular scaffold: A systematic review and meta-analysis. *JACC Cardiovasc Interv* 9:12–24.
14. Serruys PW, et al. (2016) Comparison of an everolimus-eluting bioresorbable scaffold with an everolimus-eluting metallic stent for the treatment of coronary artery stenosis (ABSORB II): A 3 year, randomised, controlled, single-blind, multicentre clinical trial. *Lancet* 388:2479–2491.
15. Sotomi Y, Suwannasom P, Serruys PW, Onuma Y (2017) Possible mechanical causes of scaffold thrombosis: Insights from case reports with intracoronary imaging. *EuroIntervention* 12:1747–1756.
16. Ortega-Paz L, et al. (2017) Predilation, sizing and post-dilation scoring in patients undergoing everolimus-eluting bioresorbable scaffold implantation for prediction of cardiac adverse events: Development and internal validation of the PSP score. *EuroIntervention* 12:2110–2117.
17. Agrawal CM, Haas KF, Leopold DA, Clark HG (1992) Evaluation of poly(L-lactic acid) as a material for intravascular polymeric stents. *Biomaterials* 13:176–182.
18. Burdick JA, Frankel D, Dernell WS, Anseth KS (2003) An initial investigation of photocurable three-dimensional lactic acid based scaffolds in a critical-sized cranial defect. *Biomaterials* 24:1613–1620.
19. Arias V, Höglund A, Odelius K, Albertsson AC (2014) Tuning the degradation profiles of poly(L-lactide)-based materials through miscibility. *Biomacromolecules* 15:391–402.
20. Wang Y (2011) US Patent 20,140,039,603 A1.
21. Schmitz KP, et al. (2009) US Patent 8,961,591 B2.
22. Tsuji H, Ikada Y (1995) Properties and morphologies of poly(l-lactide): 1. Annealing condition effects on properties and morphologies of poly(l-lactide). *Polymer (Guildf)* 36:2709–2716.
23. Cai H, Dave V, Gross R, McCarthy SP (1996) Effects of physical aging, crystallinity, and orientation on the enzymatic degradation of poly(lactic acid). *J Polym Sci, B, Polym Phys* 34:2701–2708.
24. Burg KJ, LaBerge M, Shalaby SW (1998) Change in stiffness and effect of orientation in degrading polylactide films. *Biomaterials* 19:785–789.
25. Ailianou A, Ramachandran K, Kossuth MB, Oberhauser JP, Kornfield JA (2016) Multiplicity of morphologies in poly (l-lactide) bioresorbable vascular scaffolds. *Proc Natl Acad Sci USA* 113:11670–11675.
26. Marega C, Marigo A, DiNoto V, Zannetti R (1992) Structure and crystallization kinetics of poly(L-lactic acid). *Makromol Chem* 193:1599–1606.
27. Kister G, Cassanas G, Vert M, Pauvert B, Térol A (1995) Vibrational analysis of poly(L-lactic acid). *J Raman Spectrosc* 26:307–311.
28. Tanaka M, Young RJ (2006) Molecular orientation distributions in a biaxially oriented poly(L-lactic acid) film determined by polarized Raman spectroscopy. *Biomacromolecules* 7:2575–2582.
29. Taddei P, Tinti A, Fini G (2001) Vibrational spectroscopy of polymeric biomaterials. *J Raman Spectrosc* 32:619–629.
30. Bertoluzza A, et al. (1997) Vibrational spectroscopy of biodegradable polymers. *Spectroscopy of Biological Molecules: Modern Trends*, eds Carmona P, Navarro R, Hernanz A (Springer, Dordrecht, The Netherlands), pp 507–508.
31. Damen TC, Porto SPS, Tell B (1966) Raman effect in zinc oxide. *Phys Rev* 142:570–574.
32. Oberhauser JP, Hossainy S, Rapoza RJ (2009) Design principles and performance of bioresorbable polymeric vascular scaffolds. *EuroIntervention* 5(Suppl F):F15–F22.
33. Iannace S, Maffezzoli A, Leo G, Nicolais L (2001) Influence of crystal and amorphous phase morphology on hydrolytic degradation of PLLA subjected to different processing conditions. *Polymer (Guildf)* 42:3799–3807.
34. ASTM International (2013) Standard test methods for in vitro pulsatile durability testing of vascular stents (ASTM International, West Conshohocken, PA), Standard F2477-07(2013).
35. Gaona LA, Ribelles JLG, Perilla JE, Lebourg M (2012) Hydrolytic degradation of PLLA/PCL microporous membranes prepared by freeze extraction. *Polym Degrad Stabil* 97:1621–1632.
36. Li SM, Garreau H, Vert M (1990) Structure-property relationships in the case of the degradation of massive aliphatic poly-(α-hydroxy acids) in aqueous media. *J Mater Sci Mater Med* 1:123–130.
37. Pietrzak WS, Sarver DR, Verstynen ML (1997) Bioabsorbable polymer science for the practicing surgeon. *J Craniofac Surg* 8:87–91.
38. Kolandaivelu K, et al. (2011) Stent thrombogenicity early in high-risk interventional settings is driven by stent design and deployment and protected by polymer-drug coatings. *Circulation* 123:1400–1409.
39. Jiménez JM, et al. (2014) Macro- and microscale variables regulate stent haemodynamics, fibrin deposition and thrombomodulin expression. *J R Soc Interface* 11:20131079.
40. Luo Q, et al. (2014) Degradation model of bioabsorbable cardiovascular stents. *PLoS One* 9:e110278.
41. Bobel AC, Petisco S, Sarasua JR, Wang W, McHugh PE (2015) Computational bench testing to evaluate the short-term mechanical performance of a polymeric stent. *Cardiovasc Eng Technol* 6:519–532.
42. Debusschere N, Segers P, Dubruel P, Verhegghe B, De Beule M (2015) A finite element strategy to investigate the free expansion behaviour of a biodegradable polymeric stent. *J Biomech* 48:2012–2018.
43. Fischer EW, Sterzel HJ, Wegner G (1973) Investigation of the structure of solution grown crystals of lactide copolymers by means of chemical reactions. *Colloid Polym Sci* 251:980–990.

APPLIED PHYSICAL SCIENCES

BIOPHYSICS AND COMPUTATIONAL BIOLOGY

www.manaraa.com